

Ballistic Injection Terahertz Plasma Instability in Graphene n^+i-n^+ Field-Effect Transistors and Lateral Diodes

V. Ryzhii^{*1,2}, M. Ryzhii³, A. Satou¹, V. Mitin⁴, M. S. Shur⁵, and T. Otsuji¹,

¹Research Institute of Electrical Communication, Tohoku University, Sendai 980-8577, Japan

²Institute of Ultra High Frequency Semiconductor Electronics of RAS, Moscow 117105, Russia

³Department of Computer Science and Engineering,
University of Aizu, Aizu-Wakamatsu 965-8580, Japan

⁴Department of Electrical Engineering, University at Buffalo, SUNY, Buffalo, New York 14260, USA

⁵Department of Electrical, Computer, and Systems Engineering,
Rensselaer Polytechnic Institute, Troy, New York 12180, USA

* Corresponding author: e-mail v-ryzhii(at)riec.tohoku.ac.jp, Phone+81-242-222-379

Keywords: graphene field-effect transistor, graphene lateral diode, ballistic electrons, electron drag
We analyze the operation of the graphene n^+i-n^+ field-effect transistors (GFETs) and lateral diodes (GLDs) with the injection of ballistic electrons into the n-region. The momentum transfer of the injected ballistic electrons could lead to an effective Coulomb drag of the quasi-equilibrium electrons in the n-region and the plasma instability in the GFETs and GLDs. The instability enables the generation of terahertz radiation. The obtained results can be used for the optimization of the structures under consideration for different devices, in particular, terahertz emitters.

1. INTRODUCTION

The plasma instability and the related self-excitation of plasma oscillations in two dimensional (2D) structures can lead to the generation of the terahertz (THz) radiation [1]. This effect was reported in many theoretical and experimental papers [2–5] (see also the references therein). The 2D structures with the graphene channel (G-channel) have advantages compared with those based on the standard materials. The high-energy ballistic electrons (BEs) [6–12] injected into the G-channel lead to an effective Coulomb drag of the equilibrium carriers [13–17] strongly affecting the device characteristics. As demonstrated recently [18, 19], the Coulomb interaction of the injected BEs with the quasi-equilibrium electrons (QEs) results in the dragged electrons (DEs) in the gated G-channel of the n^+i-n^+ graphene field effect transistors (GFETs) and the dragged holes (DH) in the p^+p-i-n^+ graphene tunneling transistors (GTTs) [20]. The drag effect is associated with the linearity of the electron and hole energy-momentum relations in G-channels and followed from the specifics of the kinematics of the carrier pair collisions [21–23] and can enable the plasma instability associated with the internal current amplification [14].

In this paper, we analyze the high-frequency characteristics of the n^+i-n^+ G-channel structures with the gated n-region (called as the GFETs) and with the ungated n-region, to which we refer to as the graphene lateral diodes (GLDs). The Coulomb drag in the GFETs and GLDs was considered recently [17]. We now use the distributed (waveguide) model of the electron plasma in the n-regions instead of the previous model based on the equivalent circuits with the lumped capacitance and kinetic inductance of these regions. The lumped-element model describes well the fundamental plasmonic resonance in the GFETs and GLDs. However, the consideration of the resonance harmonics and the analysis of GLDs

require the distributed model. The electron viscosity can substantially affect the plasma resonances, especially for higher harmonics. Accounting for the viscosity also requires using the distributed model. A substantial distinction of the plasma oscillations spectra in the gated and ungated channels [24–27] leads to markedly different characteristics of the GFETs and GLDs despite a similarity of the drag effect in these devices. In particular, the plasmonic resonances in the GLDs can correspond to markedly higher frequencies compared to the GFETs with the same n-region length.

Below we calculate the frequency-dependent impedance of the GFETs and GLDs as a function of the structural characteristics. We demonstrate that the real part of the impedance can be negative in the THz frequency range where the impedance imaginary part changes sign. This corresponds to the plasma instability and the self-excitation of THz plasma oscillations [28] enabling the THz radiation emission using a pertinent antenna. We calculate the growth rate of the self-excited plasma oscillation as a function of the drag factor and the device structural parameters.

The paper is organized as follows. In Sec. 2, we discuss the GFET and GLD device model describing the BE and QE transport and the role of DEs. In Sec. 3, we derive the spatial distribution of the ac potential in GFETs and calculate their frequency-dependent impedance. Section 4 deals with the calculation of the GLD frequency-dependent impedance using the 2D Poisson equation for the spatial distribution of the ac potential. Using the obtained expression for the frequency-dependent impedance, we analyze the instability of the steady-state current flow in the GFETs (the plasma instability toward the self-excitation of the coupled oscillation of the potential and the electron density) and find the instability conditions and the oscillations growth rate. In Sec. 5, the results of the distributed device model are compared with those using a lumped circuit model.

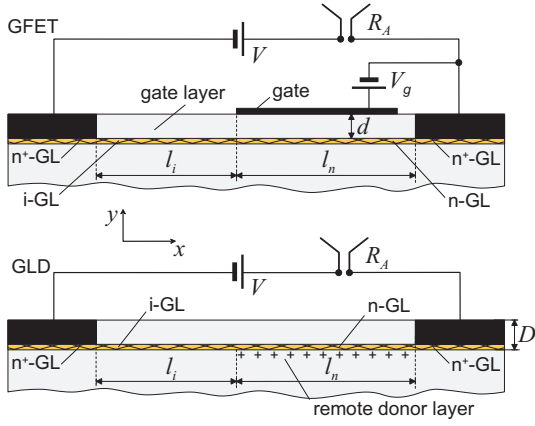


FIG. 1. Schematic view of GFET and GLD circuit with an antenna (R_A is the antenna radiation resistance).

We also comment on the role of the GLD contacts. In Sec. 6 we summarize the main conclusions.

2. DEVICE MODEL

Figure 1 shows the schematical views of the GFET and GLD under consideration. The n-region in the GFET is electrostatically induced by the gate voltage $V_g > 0$. The formation of the n-region in the GDs is due to the remote donor doping. Such a selective doping can provide the electron densities sufficient for the effective interaction with the BEs injected from the n⁺-source contact region via the i-region and for the pronounced plasmonic response without marked sacrificing of the QE mobility. Similar devices can be implemented using the p⁺-i-p-p⁺ structures and using G-multilayer gated and selectively doped structures with a commensurate improvements in performance. The GFETs and GLDs under consideration are forward biased by the source-drain dc voltage V_0 . It is assumed that the conditions of the ballistic transport of the injected BEs and the effective transfer of the BE momentum to the QEs are fulfilled. This primarily implies that the lengths, l_i and l_n , of the i- and n-regions, respectively, are not too large (in the μm range or somewhat smaller, see [17, 18] for details), providing sufficiently large Coulomb drag factor b ($b \gtrsim 1$).

Considering that the net source-drain voltage comprises the signal component $V = V_0 + \delta V_\omega \exp(-i\omega t)$ with δV_ω and ω being the signal amplitude and frequency, respectively, we obtain:

$$\delta J_\omega^{BE} = \frac{\sigma_i \delta \varphi_\omega}{l_i} \Big|_{x=0}, \quad \delta J_\omega^{QE} = \sigma_n \frac{i\nu_n}{(\omega + i\nu_n)} \frac{d\delta \varphi_\omega}{dx}. \quad (1)$$

Here the density of the BE ac current across the i-region ($-l_i \leq x \leq 0$) and the density of the QE ac current in the n-region ($0 \leq x \leq l_n$), respectively, $\sigma_i = \kappa v_W / 2\pi$ is the conductivity of the i-region (disregarding the BE transit-time delay), $\sigma_n = (e^2 \mu_n / \pi \hbar^2 \nu_n)$ is the n-region Drude dc

conductivity, κ is the effective dielectric constant of the media surrounding the G-channel, $v_W \simeq 10^8$ cm/s is the characteristic electron velocity in G-channels, τ_n is the QE momentum relaxation time ($\nu_n = \tau_n^{-1}$ represents the frequency of the QE collisions with impurities and acoustic phonons), μ_n and Σ_n are the QE Fermi energy and density with $\mu_n \simeq \hbar v_W \sqrt{\pi \Sigma_n}$, e is the electron charge, \hbar is the Planck constant, and $\delta \varphi_\omega = \delta \varphi_\omega(x, y)|_{y=0}$ expresses the ac potential spatial distribution along the axis x directed in the G-channel plane ($y = 0$) with $x = -l_i$ and $x = l_n$ corresponding to the coordinate of the n⁺-source and drain region, respectively. The frequency dependence of the ac conductance reflects the kinetic inductance of the QE system.

The DE ac current is given by [17, 18]

$$\delta J_\omega^{DE} = b\Lambda \delta J_\omega^{BE}, \quad (2)$$

where b is the drag factor [16, 17], $b\Lambda = dJ_0^{DE}/dJ_0^{BE}$, $J_0^{BE} = \sigma_i \Phi_0 / l_i$ is the dc bias current, and Φ_0 is the dc potential at $x = 0$ corresponding to the bias voltage V_0 .

3. GFET IMPEDANCE SPECTRAL CHARACTERISTICS

The standard procedure of reducing of the general system of electron plasma hydrodynamic equations coupled with the 2D Poisson equation [29–32] using in the gradual channel approximation [33] yields the spatial distribution of the ac potential $\delta \varphi_\omega = \delta \psi_\omega(x, y)|_{y=0}$, where $\delta \psi(x, y)$ is the potential around the n-region of the G-channel ($y = 0$), by the following equation (see, for example, [29]):

$$\frac{d^2 \delta \varphi_\omega}{dx^2} + \frac{\omega(\omega + i\nu_n)}{s^2} (\delta \varphi_\omega - \delta V_\omega) = 0 \quad (3)$$

with the boundary conditions at the edges of the n-region: $\delta \varphi_\omega|_{x=0} = l_i \delta J_\omega^{BE} / \sigma_i$ and $\delta \varphi_\omega|_{x=l_n} = \delta V_\omega$, δJ_ω^{BE} coincides with the net ac terminal current. These boundary conditions are valid for all devices under consideration. The plasma velocity in the gated n-region is given by $s = \sqrt{4e^2 \mu_n d / \kappa \hbar^2}$ with $d \ll l_n$ being the thickness of the layer separating the gate and the n-region of the channel. In reality, the electron fluid viscosity (see also [34–36]) can strongly affect the electron dynamics, resulting in a strong damping of the plasma resonances, particularly, affecting the higher resonances, their height and widths [1, 34]. This is due to the deviation of the ac potential and electron density spatial distributions from a linear function. To account for the viscosity effect, we put in Eq. (3) $\nu_n = \bar{\nu}_n + \hbar k^2$ [34], where \hbar is the QE viscosity and $k = \omega/s$ is the plasma wave number. Considering that for the characteristic plasma frequency Ω^{GFET} one obtains $\Omega^{GFET}/s = \pi/2l_n$, we set $\nu_n = \bar{\nu}_n + \hbar(\pi^2/4l_n^2)(\omega/\Omega^{GFET})^2$. It is worth mention

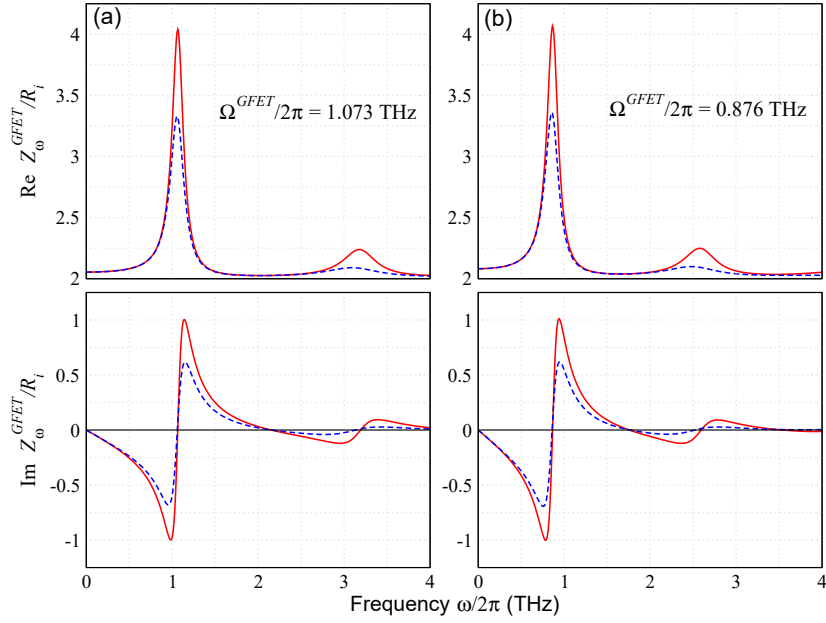


FIG. 2. Real and imaginary parts of the GFET impedance, $\text{Re } Z_{\omega}^{GFET}/R_i$ and $\text{Im } Z_{\omega}^{GFET}/R_i$, versus signal frequency $\omega/2\pi$ at weak drag effect ($b\Lambda = 0.5$): (a) $\Omega^{GFET}/2\pi = 1.073$ THz, $\eta = 9.2$, $\kappa = 4$ and (b) $\Omega^{GFET}/2\pi = 0.876$ THz, $\eta = 6.1$, $\kappa = 6$. Solid lines correspond to

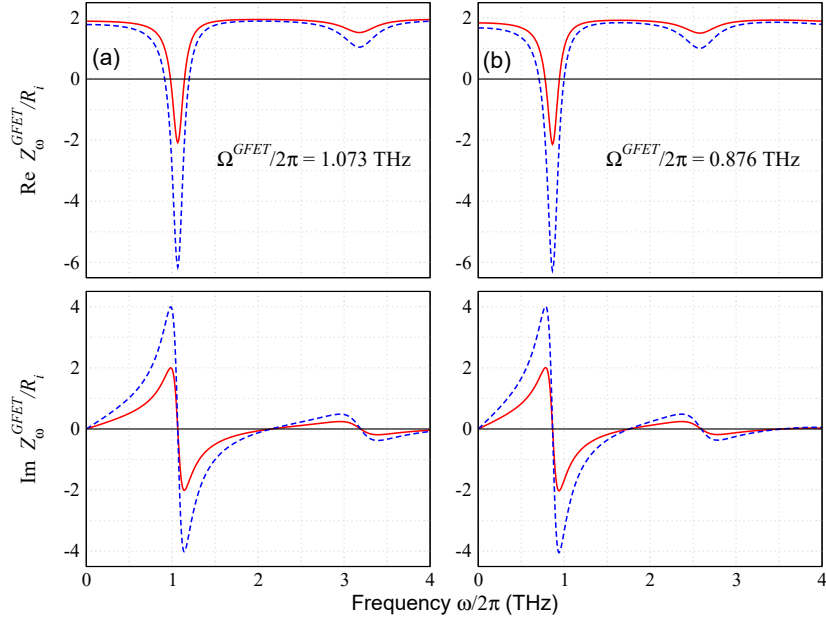


FIG. 3. Real and imaginary parts of the GFET impedance, $\text{Re } Z_{\omega}^{GFET}/R_i$ and (b) $\text{Im } Z_{\omega}^{GFET}/R_i$, versus signal frequency $\omega/2\pi$ for GFETs with (a) $\Omega^{GFET}/2\pi = 1.073$ THz, and (b) $\Omega^{GFET}/2\pi = 0.876$ THz ($h = 250$ cm²/s, $b\Lambda = 2.0$ - solid lines and $b\Lambda = 3.0$ - dashed lines).

that both the electron drag and the elevated electron viscosity in G-channels originate from the specifics of the Coulomb interaction of the 2D electrons with the linear dispersion law.

Solving Eq. (3) with the boundary conditions under consideration, we obtain

$$\delta\varphi_{\omega} - \delta V_{\omega} = (\delta\varphi_{\omega}|_{x=0} - \delta V_{\omega}) \left[\cos\left(\frac{\gamma_{\omega}^{GFET} x}{l_n}\right) - \frac{\cos(\gamma_{\omega}^{GFET})}{\sin(\gamma_{\omega}^{GFET})} \sin\left(\frac{\gamma_{\omega}^{GFET} x}{l_n}\right) \right]. \quad (4)$$

In Eq. (4),

$$\gamma_{\omega}^{GFET} = \frac{\pi\sqrt{\omega(\omega + i\nu_n)}}{2\Omega^{GFET}}, \quad (5)$$

where the plasma frequency is given by

$$\Omega^{GFET} = \frac{e}{\hbar} \sqrt{\frac{\pi^2 \mu_n d}{\kappa l_n^2}} \propto \sqrt{\frac{d}{l_n^2}}. \quad (6)$$

Substituting $\delta\varphi_{\omega}$ from Eq. (4) into Eq. (1), equalizing δJ_{ω}^{BE} and $(\delta J_{\omega}^{DE} + \delta J_{\omega}^{QE}|_{x=0})$ (i.e., using the Kirchhoff's circuit law), and accounting for the antenna radiation resistance R_A , we arrive at the following expression for the GFET impedances $Z_{\omega}^{GFET} = \delta V_{\omega}/H\delta J_{\omega} + R_A$:

$$\frac{Z_{\omega}^{GFET}}{R_i} = -i \frac{(1 - b\Lambda)}{\eta} \frac{(\omega + i\nu_n)}{\nu_n} \frac{\tan(\gamma_{\omega}^{GFET})}{\gamma_{\omega}^{GFET}} + 1 + \rho_A. \quad (7)$$

Here H is the device size in the z -direction perpendicular to the source-drain current direction (device width), $R_i = l_i/H\sigma_i$ is the i -region resistance, $\rho_A = R_A/R_i$, $\eta = R_i/R_n$ is the ratio of the n -region and i -region resistances with $R_n = l_n/H\sigma_n$, so that $\eta = l_i\sigma_n/l_l\sigma_i$. In the absence of the electron drag at ω tending to zero, Z_{ω}^{GFET} tends to $Z_0^{GFET} = R_n + R_i + R_A$.

Using the properties of the trigonometric functions [37], the GFET impedance given by Eq. (7) can be presented in the form explicitly expressing its resonant behavior:

$$\begin{aligned} \frac{Z_{\omega}^{GFET}}{R_i} &= -i \frac{8}{\pi^2} \frac{(1 - b\Lambda)}{\eta} \frac{(\omega + i\nu_n)}{\nu_n} \\ &\times \sum_{m=1}^{\infty} \frac{(\Omega^{GFET})^2}{(2m-1)^2(\Omega^{GFET})^2 - \omega(\omega + i\nu_n)} + 1 + \rho_A. \end{aligned} \quad (8)$$

As follows from Eq. (7) and more clearly seen from Eq. (8), when $\Omega^{GFET} \gg \nu_n$, the real part of the GFET impedance $\text{Re } Z_{\omega}^{GFET}$ as a function of the signal frequency ω exhibits the resonant peaks. The resonant frequencies ω_{2m-1} , where $m = 1, 2, 3, \dots$ is the resonance index, are given by

$$\omega_{2m-1} \simeq (2m-1) \sqrt{(\Omega^{GFET})^2 - \nu_n^2}. \quad (9)$$

For the height of the resonant peak we obtain

$$\left| \frac{\text{Re } Z_{\omega}^{GFET}}{R_i} \right| = \frac{8}{\pi^2} \frac{|1 - b\Lambda|}{\eta} \left(\frac{\Omega^{GFET}}{\nu_n} \right)^2 + 1 + \rho_A. \quad (10)$$

The resonant peaks are pronounced if $(\Omega^{GFET}/\nu_n)^2 \gg \eta = R_i/R_n$. Since $\Omega^{GFET} \propto l_n^{-1}$ and $R_n \propto l_n\nu_n$, the latter inequality can be satisfied when the product $l_n\nu_n$ is

sufficiently small. A marked increase in ν_n with increasing peaks index m associated with the viscosity effect, results in relatively small height of these peaks. Assuming that $h = 250 - 500 \text{ cm}^2/\text{s}$ (see the estimates for the electron viscosity [34]) and $l_n = 0.5 \mu\text{m}$, for the quantity $\tilde{\nu}_n = h(\pi^2/4l_n^2) \simeq 0.25 - 0.5 \text{ ps}^{-1}$. Using Eq. (8), at $\bar{\nu}_n = 0.75 \text{ ps}^{-1}$ $h = 250 \text{ cm}^2/\text{s}$ for the ratio of the fundamental ($m = 1$) peak height and the next peak ($m = 2$) height we obtain ~ 9 .

Figure 2 shows the spectral characteristics of the normalized real and imaginary parts of the GFET impedance, $\text{Re } Z_{\omega}^{GFET}/R_i$ and $\text{Im } Z_{\omega}^{GFET}/R_i$, calculated using Eq. (7) for different values of the plasma frequencies Ω^{GFET} and the electron viscosity h . We assumed that $\mu_n = 25 \text{ meV}$, $l_n = 0.5 \mu\text{m}$, $l_n/l_i = 5$, $d = 0.05 \mu\text{m}$, $\kappa = 4$ and 6 , $\eta = 6.1$ and -9.2 , $\bar{\nu}_n = 0.75 \text{ ps}^{-1}$, $h = (250 - 500) \text{ cm}^2/\text{s}$, $\rho_A = 1$, and $b\Lambda = 0.5$. The latter parameters correspond to $b = 0.25$ and $J_0^{BE} = 1.41 \text{ A/cm}$ and can be related to the GFETs at room temperature [17]. One can see from Fig. 2(a) that the impedance real part exhibits a series of the markedly damping resonant peaks.

Figure 3 shows thereal and imaginary parts of the GFET frequency-dependent impedance normalized by R_i under the condition of relatively strong drag effect ($b\Lambda > 1$). Other parameters are the same as for Fig. 2. One can see that at chosen parameters near the plasma resonances (fundamental) with the frequencies $\omega_1/2\pi = \Omega^{GFET}/2\pi = 1.073 \text{ THz}$ and $\omega_1/2\pi = \Omega^{GFET}/2\pi = 0.876 \text{ THz}$ the GFET impedance is negative. The impedance imaginary part changes sign at the resonant frequency, i.e., in the range where $\text{Re } Z_{\omega}^{GFET} < 0$ (around of the above resonant frequencies). However, the latter takes place only for the fundamental plasma resonance due to a strong damping associated with the viscosity.

As pointed out previously [18–20], such a situation implies the possibility of the plasma instability (see below), i.e., the self-excitation of the plasma oscillations (see, for example, [28]).

4. TWO-DIMENSIONAL POTENTIAL DISTRIBUTION IN GLD AND ITS IMPEDANCE

The potential distribution $\delta\psi_{\omega}(x, y)$ around the n -layer in the GLD is governed by the 2D Poisson equation in the following form [29–32]:

$$\frac{\partial^2 \delta\psi_{\omega}}{\partial x^2} + \frac{\partial^2 \delta\psi_{\omega}}{\partial y^2} = \frac{s^2}{\omega(\omega + i\nu_n)} \frac{\partial^2 \delta\psi_{\omega}}{\partial x^2} \cdot \delta(y), \quad (11)$$

where $\delta(y)$ is the Dirac delta-function describing thinness of the G-channel. Solving Eq. (11) considering that $\delta\psi_{\omega}(x, y) = \delta\varphi_{\omega}(x) \exp(-\gamma_{\omega}^{GLD}|y|/l_n)$, and accounting for the specifics of the current induced in the blade-like conducting electrodes [39], for the n -region admittance we obtain [30]

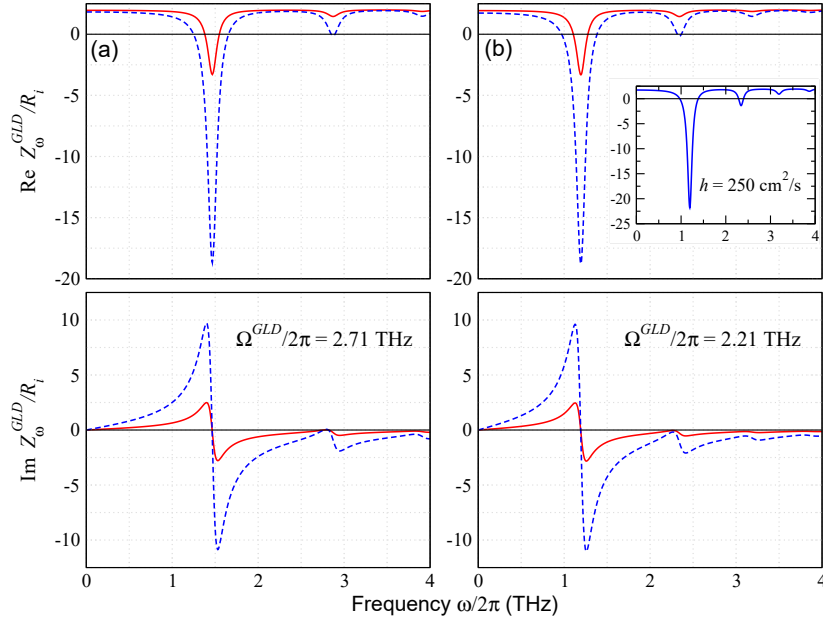


FIG. 4. Real and imaginary parts of GLD impedance, $\text{Re } Z_\omega^{GLD}/R_i$ and $\text{Im } Z_\omega^{GLD}/R_i$, versus signal frequency $\omega/2\pi$ for GLDs with (a) $\Omega^{GLD}/2\pi = 2.71$ THz, $\eta = 4.6$ and (b) $\Omega^{GLD}/2\pi = 2.21$ THz, $\eta = 3.05$ ($h = 1000$ cm^2/s , $b\Lambda = 2.0$ –solid lines and $b\Lambda = 3.0$ - dashed lines). Inset shows the $\text{Re } Z_\omega^{GLD}/r_i$ versus frequency dependence for the same parameters as in panel (b), but with smaller viscosity ($h = 250$ cm^2/s).

$$Y_\omega = i\omega \left[\frac{\kappa}{4\pi} \frac{J_0(\gamma_\omega^{GLD})}{\sin(\gamma_\omega^{GLD})} - C_l \right]. \quad (12)$$

Here

$$\gamma_\omega^{GLD} = \frac{\hbar^2 \kappa l_n \omega (\omega + i\nu_n)}{4e^2 \mu_n} = \frac{\pi \omega (\omega + i\nu_n)}{(\Omega^{GLD})^2}, \quad (13)$$

$$\Omega^{GLD} = \frac{e}{\hbar} \sqrt{\frac{4\pi \mu_n}{\kappa l_n}} \propto \sqrt{\frac{1}{l_n}}, \quad (14)$$

$J_0(\xi)$ is the Bessel function of the first kind, and C_l is the source-drain geometrical capacitance in the structures with the blade-like side contacts per unit of the GLD width. The latter, accounting for the blade-like shape of the contact is equal to $C_l \simeq (\kappa/4\pi)\mathcal{L}_l$ with $\mathcal{L}_l \sim 1$ being a logarithmic factor [39] (see also [40–42]).

Considering that

$$\delta J_\omega^{BE} = b\Lambda \delta J_\omega^{BE} + Y_\omega \left(\delta V_\omega - \frac{l_i}{\sigma_i} \delta J_\omega^{BE} \right), \quad (15)$$

for the GLD impedance Z_ω^{GLD} we arrive at the following expression:

$$\begin{aligned} \frac{Z_\omega^{GLD}}{R_i} &= \frac{(1 - b\Lambda)}{R_i Y_\omega} + 1 + \rho_A \\ &= -i \frac{(1 - b\Lambda)}{\eta \left[\frac{J_0(\gamma_\omega^{GLD})}{\sin(\gamma_\omega^{GLD})} - 1 \right]} \left[\frac{(\Omega^{GLD})^2}{\pi \omega \nu_n} \right] + 1 + \rho_A, \end{aligned} \quad (16)$$

where $t_i = R_i C_l \simeq (\kappa R_i/2\pi)\mathcal{L}_l = l_i/v_W$. When $b\Lambda$ and ω tend to zero, Y_ω and Z_ω^{GLD} tend to $Z_0^{GLD} = R_n + R_i + R_A$. In the high-frequency limit, $Z_\omega^{GLD} \simeq R_i + R_A + i/\omega C_l \simeq R_i + R_A$.

Figure 4 shows the spectral characteristics of the GLD impedance calculated using Eq. (16) for GLDs with different resonant plasma frequencies (due to different k) at different value of the drag parameter $b\Lambda$ ($b\Lambda > 1$) assuming that $\mu_n = 25$ meV, $l_n = 1.0$ μm , $l_n/l_i = 10$, $\kappa = 4 - 6$, $\eta = 6.1 - 9.2$, $\bar{\nu}_n = 0.75$ ps^{-1} , $\rho_A = 1$, and $h = 1000$ cm^2/s . The n-region length is chosen to be as twice as larger than that in Fig. 3 related to the GFETs. Nevertheless, the values of GLD characteristic plasma frequency Ω^{GLD} are larger than the frequency Ω^{GFET} due to the difference of these frequencies dependences on l_n and d . It also assumed that in GLD the viscosity is four times larger to provide the same value of $\bar{\nu}_n$ as for the GLD.

As seen from Fig. 4, at sufficiently large $b\Lambda$ the impedance real part $\text{Re } Z_\omega^{GLD}$ exhibits deep minima at certain frequencies. In the first minima $\text{Re } Z_\omega^{GLD} < 0$. The second minimum $\text{Re } Z_\omega^{GLD}$ is small being, nevertheless, positive. The latter is attributed to a relatively strong plasma oscillation damping due to the viscosity effect. The frequency dependences, including the magnitudes in the minima, shown in Figs. 4(a) and 4(b) appears to be rather similar, except for the values of the frequencies $\omega_1/2\pi$ and $\omega_2/2\pi$ corresponding to the $\text{Re } Z_\omega^{GLD}$ minima. These frequencies, $\omega_1/2\pi \simeq 1.5$ THz and $\omega_2/2\pi \simeq 2.9$ THz [for the GLD with $\Omega^{GLD}/2\pi = 2.71$ THz, see Fig. 4(a)] and to the minima

$\omega_1/2\pi \simeq 1.2$ THz and $\omega_2/2\pi \simeq 2.35$ THz [for the GLD with $\Omega^{GLD}/2\pi = 2.21$ THz, see Fig. 4(b)], are smaller than the pertinent values of the characteristic frequencies $\Omega^{GLD}/2\pi$ and $3\Omega^{GLD}/2\pi$. This can be explained by a substantial contribution of the GLD geometrical capacitance to the plasma resonances. Such a capacitance increases the net capacitance in comparison with the electron capacitance of the n-region (which determines Ω^{GLD}). As in the GFETs, the impedance imaginary part $\text{Im } Z_\omega^{GLD}$ changes its sign at the frequencies corresponding to the real part minima. Generally, the spectral characteristics of Z_ω^{GLD} are qualitatively similar to those of the GFETs. However, there are the following distinctions: (a) the GLD characteristic and the resonant frequencies are larger than those of the GFETs for the same n-region length, (b) the resonant frequencies in the GLDs are markedly smaller than the characteristic frequencies (while in the GFETs these frequencies are rather close to each other), and (c) the resonant peaks in the GLDs are affected by the viscosity effect for a lesser degree. Indeed, the plots in Fig. 4, are akin to the plots in Fig. 3, although the former ones exhibit deeper minima despite plotted for a much larger viscosity ($h = 1000$ cm²/s compared with $h = 250$ cm²/s used for Fig. 3). The point is that the wave numbers of the plasma oscillations in the GLDs are smaller than in the GFETs at the same frequencies.

However, as shown in the inset in Fig. 4(b), $\text{Re } Z_\omega^{GLD}$ can be negative at the frequency of the second plasma resonance $\omega_2/2\pi \simeq 2.35$ THz at a smaller, but realistic viscosity values.

Generally, the specifics of the Z_ω^{GLD} spectral characteristics implies that the GLD can exhibit the plasma instability analogously to the GFETs.

4. PLASMA INSTABILITY

We focus below of the instability in the GFETs since the spectral characteristics of the GFET and GLD impedance are qualitatively similar (negative real part and changing sign imaginary part), both corresponding to the possibility of the plasma instability,

To find the conditions of the plasma instability in the GFETs, the frequency of the self-excited modes ω' , and their growth rate ω'' corresponding to the plasma instability in the GFETs, we use the dispersion equation governing the plasma oscillation in the following form: $Z_{\omega'+i\omega''}^{GFET} = 0$. Invoking Eq. (7) and setting $\text{Re } Z_{\omega'+i\omega''}^{GFET} = 0$ and $\text{Im } Z_{\omega'+i\omega''}^{GFET} = 0$, for the growth rate of the fundamental plasma mode we find

$$\omega'' \simeq -\frac{\nu_n}{2} \left[1 + \frac{8}{\pi^2} \frac{(1-b\Lambda)}{\eta(1+\rho_A)} \left(\frac{\Omega^{GFET}}{\nu_n} \right)^2 \right]. \quad (17)$$

If $b\Lambda < 1$ (no electron drag or a weak electron drag), Eq. (17) yields $\omega'' < 0$. This corresponds to the damping

of the plasma oscillations with the frequency $\simeq \Omega^{GFET}$. At $b\Lambda = 0$, i.e., in the absence of the electron drag, and $R_A = 0$, Eq. (17) yields $\omega'' = -\nu_n/2 + t_{RC}^{-1}$, where $t_{RC} = R_i C_n$ is the time of the gated the n-region recharging via the i-region (with the resistance R_i , see above).

However, if

$$b\Lambda > 1 + \frac{\pi^2 \eta (1 + \rho_A)}{8} \left(\frac{\nu_n}{\Omega^{GFET}} \right)^2, \quad (18)$$

the amplitude of the plasma oscillations is growing, i.e., the plasma instability takes place. When $\nu_n \ll \Omega^{GFET}$, inequality (19) can be satisfied at much smaller $b\Lambda$ than required for the GFET source-drain characteristics of the S-type [17]. Considering that $b\Lambda \simeq 4\pi e l_i J_0^{BE} / \kappa v_W \mu_n$ [17], inequality (18) can be presented as

$$J_0^{BE} > J_{th}^{BE} = \bar{J}_{th}^{BE} \left[1 + \frac{\pi^2 \eta (1 + \rho_A)}{8} \left(\frac{\nu_n}{\Omega^{GFET}} \right)^2 \right], \quad (19)$$

where

$$\bar{J}_{th}^{BE} = \left(\frac{\kappa v_W \mu_n}{4\pi e l_i} \right). \quad (20)$$

For typical parameters $\kappa = 4 - 6$, $l_i = 0.1$ μm , $l_n = 0.5$ μm , $d = 5 \times 10^{-6}$ cm, $\mu_n = 25$ meV, $\nu_n = 1$ ps⁻¹, and $\rho_A = 1$, we arrive at the following estimates: $\eta \simeq 6 - 9$, $\Omega^{GFET}/2\pi = 0.87 - 1.08$ THz, and $J_{th}^{BE} \simeq (130 - 190)$ mA/cm. The latter values of the threshold dc current are markedly smaller than that at which the emission of optical phonons by the BEs (affecting the GFET characteristics) becomes essential [$J_0 = \kappa v_W \hbar \omega_0 / 2\pi e l_i \simeq (1410 - 2115)$ mA/cm, where $\hbar \omega_0 \simeq 200$ meV is the optical phonon energy [16, 18]].

The electron viscosity leads to a strong damping of the higher plasma oscillation harmonics. This results in larger values of $b\Lambda$ and J_{th}^{BE} (because of a larger ν_n) and complicates (or prevents) the appearance of the plasma instability with the self-excitation of these harmonics.

5. COMMENTS

Distributed model versus lumped-element model

Compare the GFET impedance calculated using the lumped capacitance and inductance model with that obtained above. The latter is given by (in the present notations) [18]

$$\frac{Z_\omega}{R_i} = \frac{(1-b\Lambda)}{\eta(1+i\mathcal{F}_\omega)} \frac{(\omega^2 + \nu_n^2)}{\nu_n^2} + 1 + \rho_A, \quad (21)$$

where $\mathcal{F}_\omega = (\omega/\nu_n)[(\Omega_l^{GFET})^2 - \omega^2 - \nu_n^2]/(\Omega_l^{GFET})^2$ with Ω_l^{GFET} , which differs from Ω^{GFET} given by Eq. (6) by

a factor of $\sqrt{2/\pi}$. This is because the distributed model accounts for a deviation of the ac potential distribution in the n-region from a linear distribution (in contrast to the lumped-element model). Equation (21) yields the resonant peak height equal to the fundamental resonant peak ($m = 1$) height described by Eq. (10). However, the main distinction in the spectral characteristics of the GFET impedance calculated by the distributed and lumped-element models is that the former can describe a multiple peak structure.

Effect of the side contacts shape on the plasma resonances in GLDs

Equations (12) - (14) correspond to the case of the GLDs with the blade-like side contacts. If the thickness of the side contacts in the GLDs, $D > l_i + l_n \simeq l_n$ (the GLDs with bulk contacts), we have to account for the features of the displacement current induced by the carriers between the source and drain (bulk) contacts. In this case, for the n-region admittance we obtain [compare with Eq. (12)]

$$Y_\omega = i \left(\frac{\sigma_n \nu_n}{\omega + i\nu_n} - \omega C_b \right). \quad (22)$$

We estimate the capacitance C_b as $C_b \sim (\kappa/4\pi)\mathcal{L}_b$ with $\mathcal{L}_b \sim D/l_n$. In the case under consideration, Eqs. (15) and (22) lead to the following formula for Z_ω^{GLD} :

$$\begin{aligned} \frac{Z_\omega^{GLD}}{R_i} &= -i \frac{(1 - b\Lambda)}{\frac{\omega t_i \mathcal{L}_b}{2} \left[\frac{4\pi \sigma_n \nu_n}{\mathcal{L}_b \kappa l_n \omega (\omega + i\nu_n)} - 1 \right]} + 1 + \rho_A \\ &= -i \frac{(1 - b\Lambda)}{\frac{\omega t_i \mathcal{L}_b}{2} \left[\frac{(\Omega_b^{GLD})^2}{\omega (\omega + i\nu_n)} - 1 \right]} + 1 + \rho_A, \end{aligned} \quad (23)$$

Hence $t_i \mathcal{L}_b \simeq (l_i/\nu_W)(D/l_n) = t_i(D/l_n)$ and the plasma frequency in the GDs with bulk contacts is given by

$$\Omega_b^{GLD} \simeq \frac{e}{\hbar} \sqrt{\frac{4\mu_n}{\kappa l_n \mathcal{L}_b}} \sim \frac{e}{\hbar} \sqrt{\frac{4\mu_n}{\kappa D}}. \quad (24)$$

Equation (24) can be presented in the form of Eq. (21) with \mathcal{F}_ω including Ω_b^{GLD} instead of Ω_l^{GFET} with $\Omega_b^{GLD}/\Omega_l^{GFET} = l_n/\sqrt{2dD}$ (i.e., $\Omega_b^{GLD}/\Omega^{GFET} = 2l_n/\pi\sqrt{dD}$). Thus, our model for the GLDs with relatively thick contacts yields the results similar to those obtained in the framework of the GFET lumped-element model, corresponding, in particular, to a single plasmonic resonance. However, the resonant plasma frequencies are different due to a difference of the geometrical gate capacitance in the GFET and the source-drain geometric capacitance of the GLDs with bulk contacts.

Output THz power

To estimate the maximum output THz power, one can determine the variation $\delta\Lambda$ of the parameter Λ and hence the swing of the dc bias current ΔJ_0^{BE} corresponding to $\text{Re } Z_\omega^{GFET} < 0$ (or $\text{Re } Z_\omega^{GLD} < 0$). From Eqs. (7) we find

$$b\Delta \simeq (b\Lambda - 1) + \eta(\nu_n/\Omega^{GFET})^2(1 + \rho_A). \quad (25)$$

At the parameters used for Fig. 3(a), we obtain $\eta(\nu_n\Omega^{GFET})^2 \simeq 0.2$. Considering that at $J_0^{BE} \leq J_0$ (we disregard the case or relatively high dc bias current at which the optical phonon emission markedly affects the GFET (GLD) characteristics), $\Delta\Lambda = 2\Delta J_0^{BE}/J_0$, for $b\Lambda = 2$ and $b\Lambda = 3$ [as in Fig. 3(a)], from Eq. (25) we obtain $\Delta J_0^{BE}/J_0 \simeq 0.6 - 0.7$. Considering that at the above parameters $J_0 \simeq 1.4$ A/cm and for the GFET width $H = (10 - 14)$ μm $R_i = R_A \simeq 100 - 140$ Ohm, one can obtain $\Delta J_0^{BE} \simeq (0.85 - 1.4)$ mA. In this case the maximum output THz power P_ω^{GFET} at the frequency $\omega/2\pi = 1$ THz is estimated as $P_\omega \simeq 100 - 200$ μW . Similar estimates can be obtained for the GLDs.

6. CONCLUSIONS

Our calculations of the frequency dependencies of the n⁺-i-n-n⁺ and GFETs and GLDs impedances accounting for the resonant response of the electron plasma in the n-regions, damping of the plasma oscillations due to the electron viscosity, and the Coulomb drag of the QEs by the injected BEs show that the impedance real part $\text{Re } Z_\omega$ in both GFETs and GLDs can be negative if the drag effect is sufficiently strong. Since in the frequency range, where $\text{Re } Z_\omega < 0$, $\text{Im } Z_\omega$ changes sign, i.e., turns zero at a certain THz signal frequency, the electron plasma can be unstable toward the self-excitation of the plasma oscillations (the effect of the plasma instability). This can enable the emission of the THz radiation. The electron viscosity can effectively suppress the higher plasma resonances, although this effect is weaker in the GLDs in comparison with the GFETs. The results related to the GFETs confirm the predictions obtained using a simplified model of the gated n-region as a plasmonic cavity except not accounting for the possibility of the plasma frequency harmonics self-excitation. We demonstrated that the GLDs with the ungated n-region formed by chemical selective doping can also exhibit the plasma instability and generation of the THz radiation. In these devices, the plasma resonant frequency and, hence, the frequency of the emitted THz radiation, can markedly exceed that in the GFETs for the same n-region length. The obtained results imply that the n⁺-i-n-n⁺ GFETs and GLDs can be used in novel THz radiation sources. A similar instability could also occur in p⁺-i-p-p⁺ (including the structures based on G-multilayers

with the carriers induced by the gate voltage [43] or doping) and the $p^+p\text{-}i\text{-}n\text{-}n^+$ single G-layer (i.e., GTTs [20]) or G-multilayer [44] structures with the Zener-Klein interband tunneling generation of ballistic carriers.

ACKNOWLEDGMENTS

The work at RIEC and UoA was supported by Japan Society for Promotion of Science (KAKENHI Grants No. 21H04546 and No. 20K20349), Japan; A01No. H31/A01. The work at RPI was supported by Office of Naval Research (N000141712976, Project Monitor Dr. Paul Maki).

-
- [1] M. I. Dyakonov and M. S. Shur, *IEEE Trans. Electron Devices* **1996**, 43, 1640.
- [2] G. R. Aizin, J. Mikalopas, and M. Shur, *Phys. Rev. B* **2020**, 101, 245404.
- [3] V. Ryzhii, T. Otsuji, and M. S. Shur, *Appl. Phys. Lett.* **2020**, 116, 140501.
- [4] T. Otsuji, T. Watanabe, S. A. Boubanga Tombet, A. Satou, W. M. Knap, V. V. Popov, M. Ryzhii, and V. Ryzhii, *IEEE Trans. Terahertz Sci. Technol.* **2013**, 3, 63.
- [5] D. Yadav, S. Boubanga-Tombet, T. Watanabe, S. Arnold, V. Ryzhii, and T. Otsuji, *2D Matter.* **2016**, 3, 045009.
- [6] M. S. Shur and L. F. Eastman, *IEEE Trans. Electron Devices* **1979**, 26, 1677.
- [7] K. Hess, *IEEE Trans. Electron Devices*, **1981**, 28, 937.
- [8] V. I. Ryzhii, N. A. Bannov, and V. A. Fedirko, *Sov. Phys. Semicond.* **1984**, 18, 481.
- [9] J. Xu and M. Shur, *J. Appl. Phys.* **1987**, 62, 3816.
- [10] S. E. Laux, A. Kumar, and M. V. Fischetti, *J. Appl. Phys.* **2004**, 95, 5545.
- [11] A. S. Mayorov, R. V. Gorbachev, S. V. Morozov, L. Britnell, R. Jalil, L. A. Ponomarenko, P. Blake, K. S. Novoselov, K. Watanabe, T. Taniguchi, and A. K. Geim, *Nano Lett.* **2011**, 11, 2396.
- [12] L. Banszerus, M. Schmitz, S. Engels, M. Goldsche, K. Watanabe, T. Taniguchi, B. Beschoten, and C. Stampfer, *Nano Lett.* **2016**, 16, 1387.
- [13] J. C. Song, D. A. Abanin, and L. S. Levitov, *Nano Lett.* **2013**, 13, 3631.
- [14] M. Schütt, P. M. Ostrovsky, M. Titov, I. V. Gornyi, B. N. Narozhny, and A. D. Mirlin, *Phys. Rev. Lett.* **2013**, 110, 026601.
- [15] R. V. Gorbachev, A. K. Geim, M. I. Katsnelson, K. S. Novoselov, T. Tudorovskiy, I. V. Grigorieva, A. H. MacDonald, S. V. Morozov, K. Watanabe, T. Taniguchi, and L. A. Ponomarenko, *Nat. Phys.* **2012**, 8, 896.
- [16] V. Ryzhii, M. Ryzhii, V. Mitin, M. S. Shur, and T. Otsuji, *Phys. Rev. Appl.* **2021**, 16, 014001.
- [17] V. Ryzhii, T. Otsuji, M. Ryzhii, V. Mitin, and M. S. Shur, *Phys. Status Solidi A* **2021**, 2100535.
- [18] V. Ryzhii, M. Ryzhii, V. Mitin, M. S. Shur, and T. Otsuji, *Appl. Phys. Lett.* **2021**, 119, 093501.
- [19] M. Ryzhii, V. Ryzhii, T. Otsuji, V. Mitin, and M. S. Shur, 2021 IEEE Int. Conf. Microwaves, Antennas, Communication, and Electronic Systems (COMCAS), Tel Aviv, Israel, 2021.
- [20] V. Ryzhii, M. Ryzhii, A. Satou, T. Otsuji, V. Mitin, and M. S. Shur, arXiv: 2109.00773v1 [cond-mat.mes-hall].
- [21] V. Vyurkov and V. Ryzhii, *JETP Lett.* **2008**, 88, 370.
- [22] X. Li, E. A. Barry, J. M. Zavada, M. Buongiorno Nardelli, and K. W. Kim, *Appl. Phys. Lett.* **2010**, 97, 082101.
- [23] D. Svintsov, V. Vyurkov, V. Ryzhii, and T. Otsuji, *Phys. Rev. B* **2013**, 88, 245444.
- [24] A. V. Chaplik, *Sov. Phys. JETP* **1972**, 35, 395.
- [25] V. Ryzhii, *Jpn. J. Appl. Phys.* **2006**, 45, L923.
- [26] L. A. Falkovsky and A. A. Varlamov, *European Phys. J. B* **2007**, 56, 281.
- [27] V. Ryzhii, A. Satou, and T. Otsuji, *J. Appl. Phys.* **2007**, 101, 024509.
- [28] G. I. Haddad, J. R. East, and H. Eisele, *Int. J. High Speed Electron. Syst.* **2003**, 13, 395.
- [29] A. Satou, V. Ryzhii, I. Khmyrova, M. Ryzhii, and M. S. Shur, *J. Appl. Phys.* **2004**, 95, 2084.
- [30] V. Ryzhii, A. Satou, and M. S. Shur, *J. Appl. Phys.* **93**, 93, 10041 (2003).
- [31] V. Ryzhii, A. Satou, I. Khmyrova, A. Chaplik, and M. S. Shur, *J. Appl. Phys.* **2004**, 96, 7625.
- [32] A. Satou, V. Ryzhii, and A. Chaplik, *J. Appl. Phys.* **2005**, 98, 034502.
- [33] M. Shur, *Physics of Semiconductor Devices* (Prentice-Hall, London, 1990).
- [34] Y. Zhang and M. S. Shur, *J. Appl. Phys.* **2021**, 129, 053102.
- [35] A. I. Berdyugin, S. G. Xu, F. M. D. Pellegrino, R. K. Kumar, A. Principi, I. Torre, M. B. Shalom, T. Taniguchi, K. Watanabe, I. V. Grigorieva, M. Polini, A. K. Geim, and D.A. Bandurin, *Science* **2019**, 364, 162.
- [36] A. Principi, G. Vignale, M. Carrega, and M. Polini, *Phys. Rev. B* **2016**, 93, 125410.
- [37] I. S. Gradshtain and I. M. Ryzhik, *Tables of Integrals, Series, and Products*, (Academic Press, New York, 1994)
- [38] V. Ryzhii and G. Khrenov, *IEEE Trans. Electron Devices* **1995**, 42, 166.
- [39] V. Ryzhii, A. Satou, I. Khmyrova, M. Ryzhii, T. Otsuji, V. Mitin, and M. S. Shur, *J. Phys. Conf. Ser.* **2005**, 38, 228.
- [40] S. G. Petrosyan and A. Ya. Shik, *Sov. Phys. -JETP* **1989**, 69, 2119.
- [41] B. L. Gelmont, M. S. Shur, and C. Moglestue, *IEEE Trans. Electron Devices* **1992**, 39, 1216.
- [42] D. B. Chklovskii, B. I. Chklovskii, and L. I. Glasman, *Phys. Rev. B* **1992**, 46, 4026.
- [43] M. Ryzhii, V. Ryzhii, T. Otsuji, V. Mitin, and M. S. Shur, *Phys. Rev. B* **2010**, 82 (2010).
- [44] V. L. Semenenko, V. G. Leiman, A. V. Arsenin, V. Mitin, M. Ryzhii, T. Otsuji, and V. Ryzhii, *J. Appl. Phys.* **2013**, 113, 024503.